JOURNAL OF APPLIED CRYSTALLOGRAPHY

Volume 51 (2018)

Supporting information for article:

A fast X-ray diffraction-based method for the determination of crystal size distributions (FXD-CSD)

Sigmund H. Neher, Helmut Klein and Werner F. Kuhs

A fast X-ray diffraction-based method for the determination of crystal size distributions (FXD-CSD).

Authors

Sigmund H. Neher[a]*, Helmut Klein[a] and Werner F. Kuhs[a]*

[a]GZG Crystallography, University of Göttingen, Goldschmidtstr.1, Göttingen, 37077, Germany

Correspondence email: sneher@gwdg.de; wkuhs1@gwdg.de

S1. Supporting figures

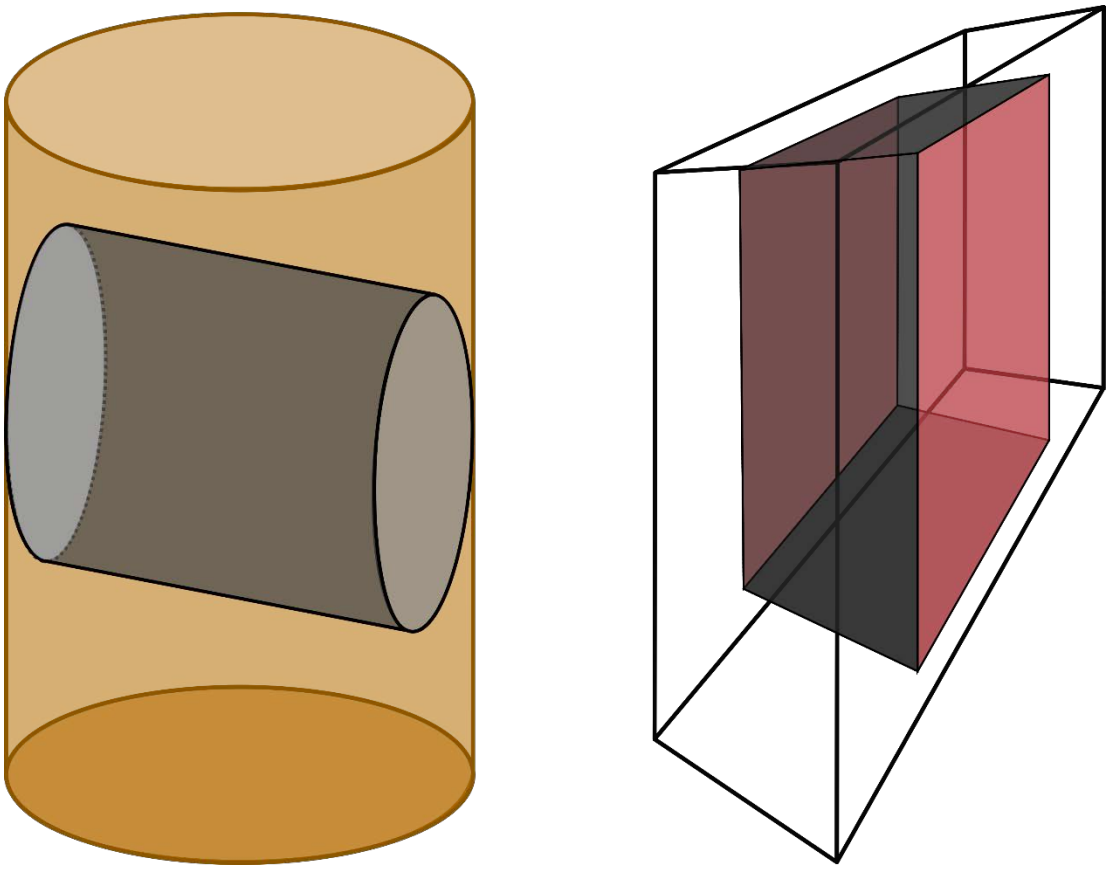

Figure S1 Irradiated sample volume (ISV) examples for different specimen types and incident beam geometries. Left: Kapton capillary filled with powder hit by a circular incident beam (pinhole collimator). Only the dark gray area contributes to the sample edge effect. Right: Polycrystalline specimen hit by a rectangular collimated incident beam. The gray areas contribute to the sample edge effect. The red areas can contribute as well if they are effected by sample preparation (e.g. by cutting).

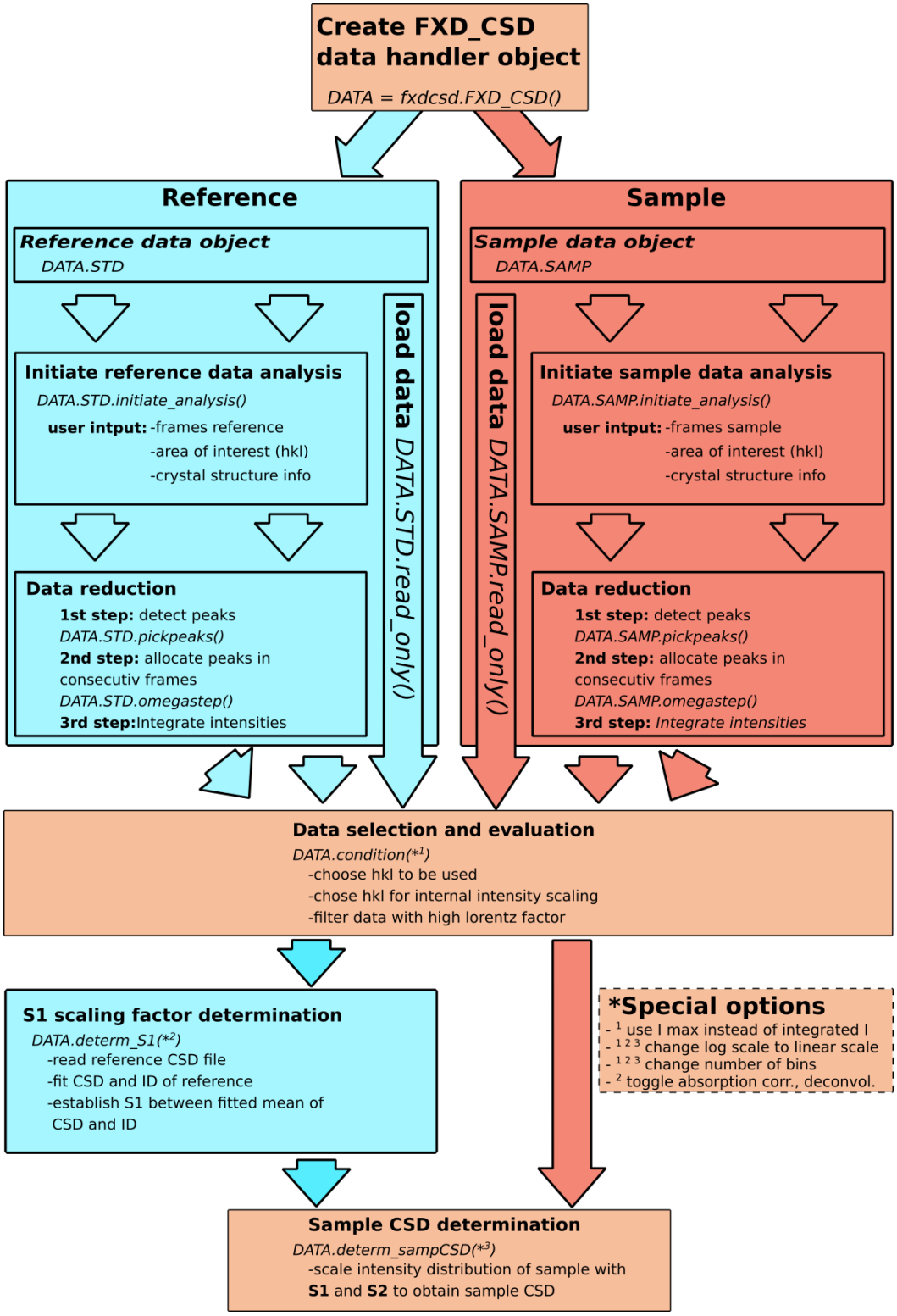

Figure S2 FXD-CSD data flow. To allow a fast and convenient data analysis the software package / module *fxdcsd* has been developed. The program, written in Python, can be run directly from the command line/terminal or executed as script. After importing the module it is executed by importing the data handler object.

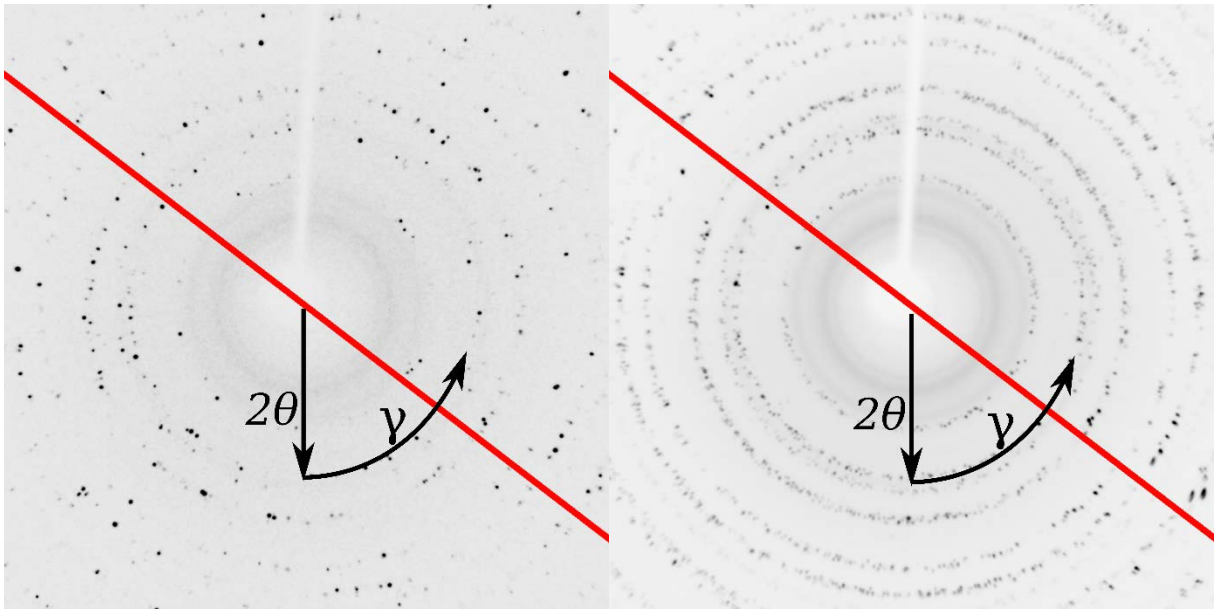

Figure S3 Effect of sample rotation during image acquisition using a 54.74° (the half octahedral dihedral angle) inclined φ-rotation axis. The red line represents the trace of the sample rotation axis on the detector. The 2θ and γ direction are indicated. Left: single frame; no apparent influence. Right: summation of several frames; reflections near the trace of the rotation axis show much higher intensities because they stay longer in diffraction state.

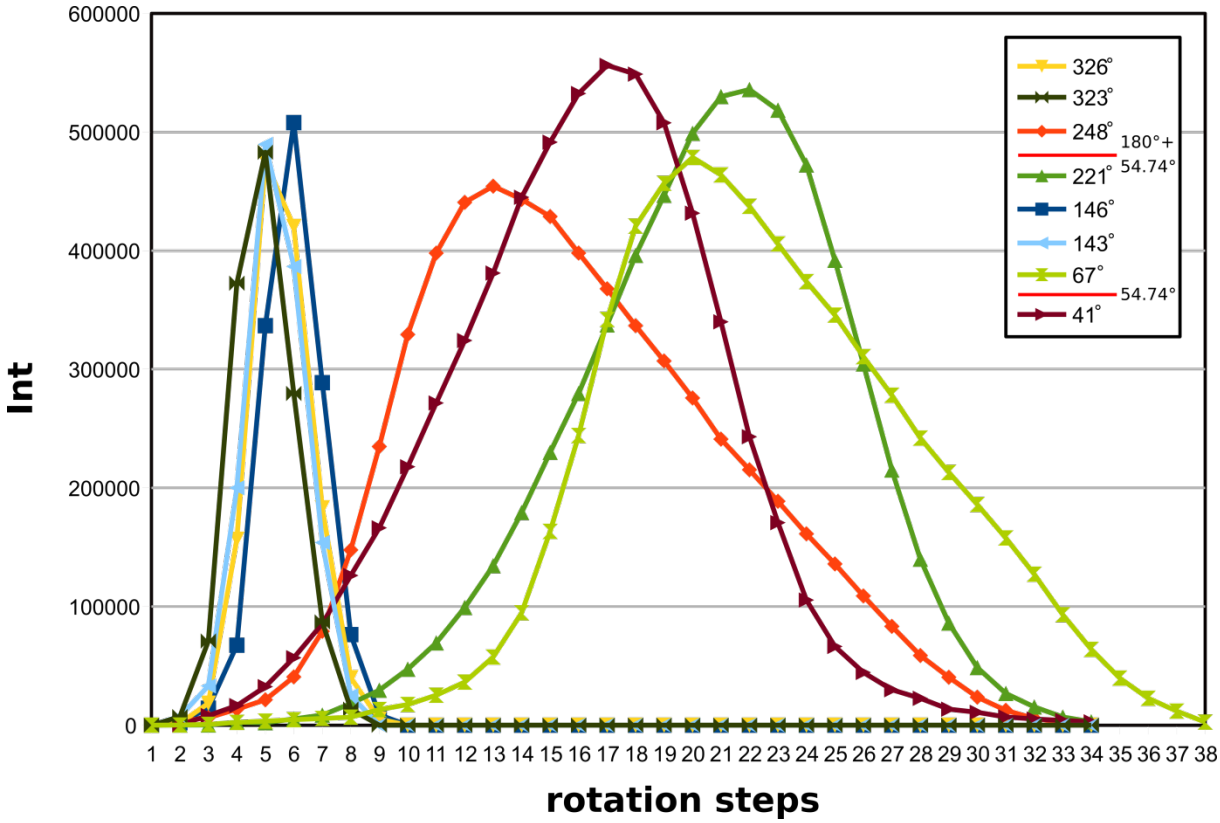

Figure S4 Rocking curves of diffraction spots intersecting the Ewald sphere with different speed due to different orientation in respect to the rotation axis γ. The data originates from a test measurement of a spherical Ylid single crystal usually used for intensity calibration. The measurement is performed in the same manner as described in §3.3 (recall Figure 2). The numbering of the coloured lines corresponds to their position on the ring, given in degree γ. The φ-rotation axis is again inclined about 54.74° in χ. Please note that the exceptional widths of some of the reflections is the sole consequence of an angular position in γ close to the nodes of the Lorentz factor correction function.

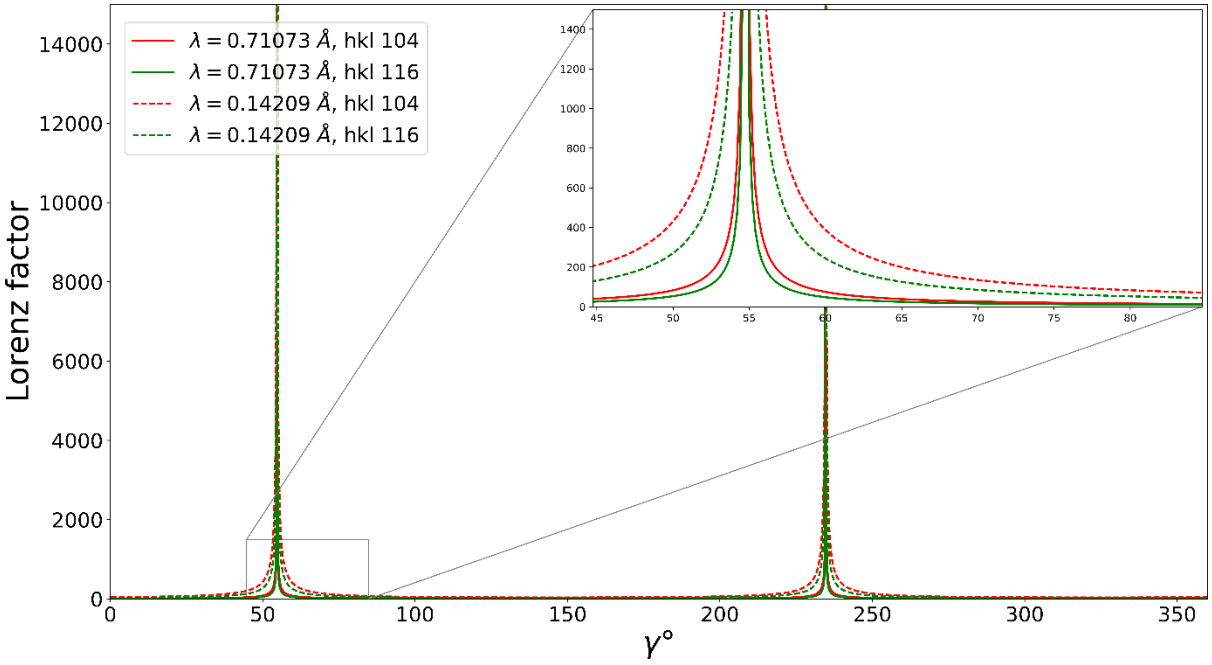

Figure S5 Lorentz factor function graph plot for two different wavelengths from simulated data. The plotted lines result from Eq. 7 in §3.5.1 fed with simulated reciprocal lattice vectors in diffraction state ($\mathbf{h}_r$), calculated from the pixel positions of 1800 evenly distributed spots on a circle. All other parameters are also inspired by a real measurement including the 54.74° inclined rotation axis. This results in the function peak at 54.74° γ. The correction factor is applied to the integrated crystal intensity. To test the correction a stepwise rotation measurement, in the FXD-CSD manner, of a spherical intensity reference Ylid single crystal was performed and verified the correctness of the applied correction (see Figure S4).

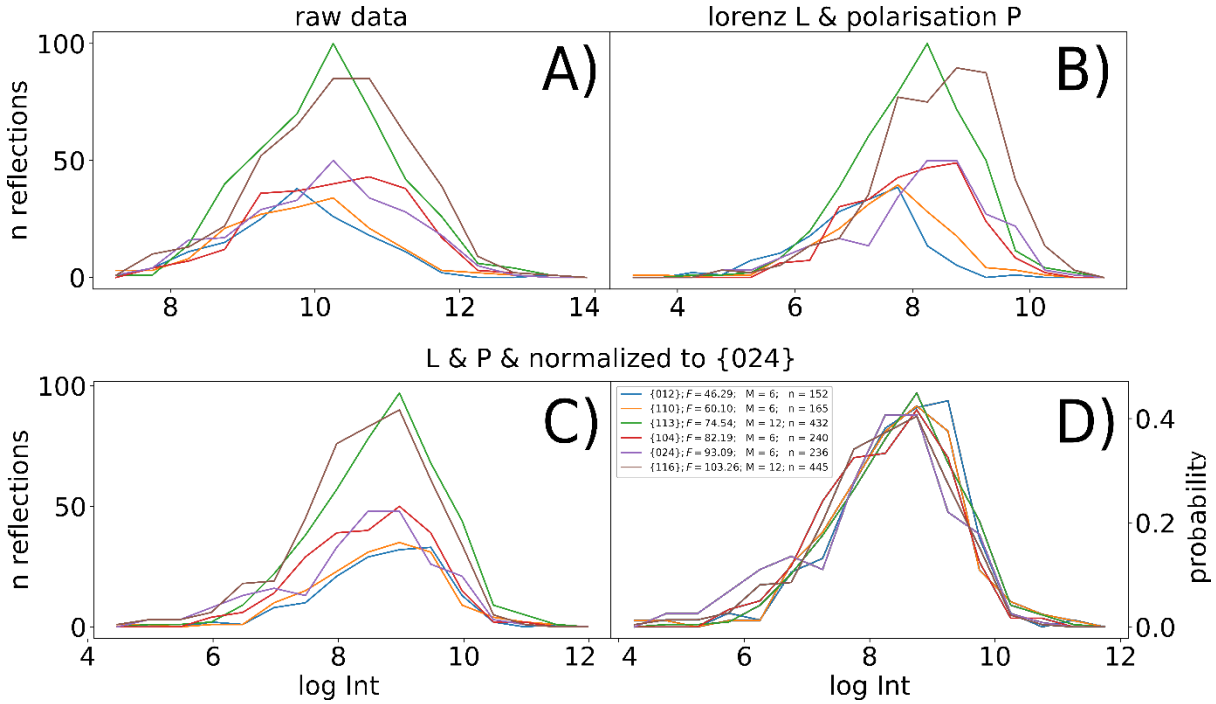

Figure S6 Subplots A-D from CSFIII, automatically produced by the *condition()* function. They show the intensity histograms from all chosen *hkl*-rings in different stages of data treatment. These are: A) the uncorrected data, B) the impact of the Lorentz and polarisation factor and the influence of the internal intensity scaling, according to the chosen structure factor. The latter is plotted as C) number of occurrence histogram and D) as probability histogram. In C) one can nicely see the effect of varying multiplicities on counting statistics. D) shows how well the measured and scaled IDs match.

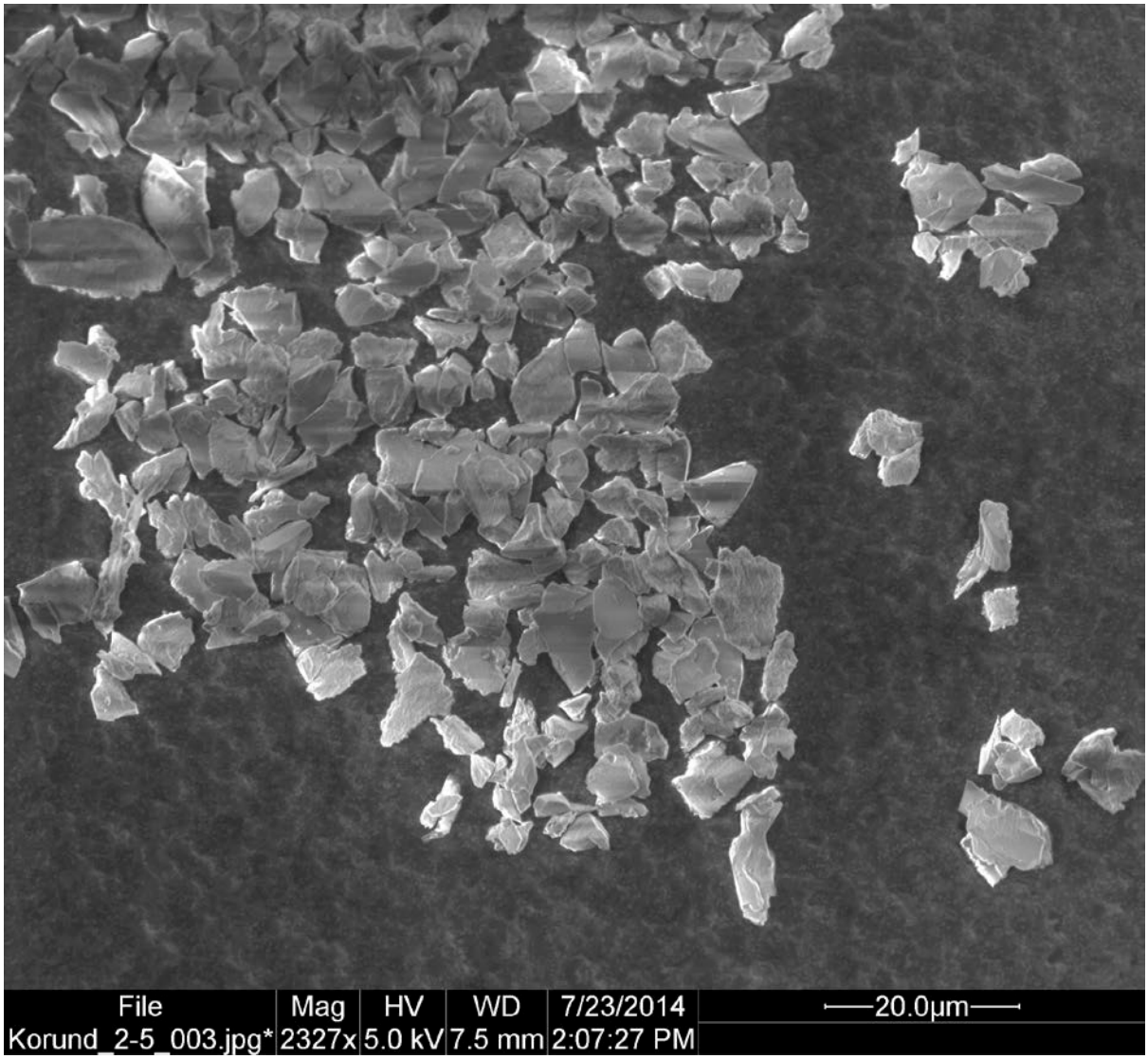

Figure S7 Example SEM image of the CSF I sample powder.

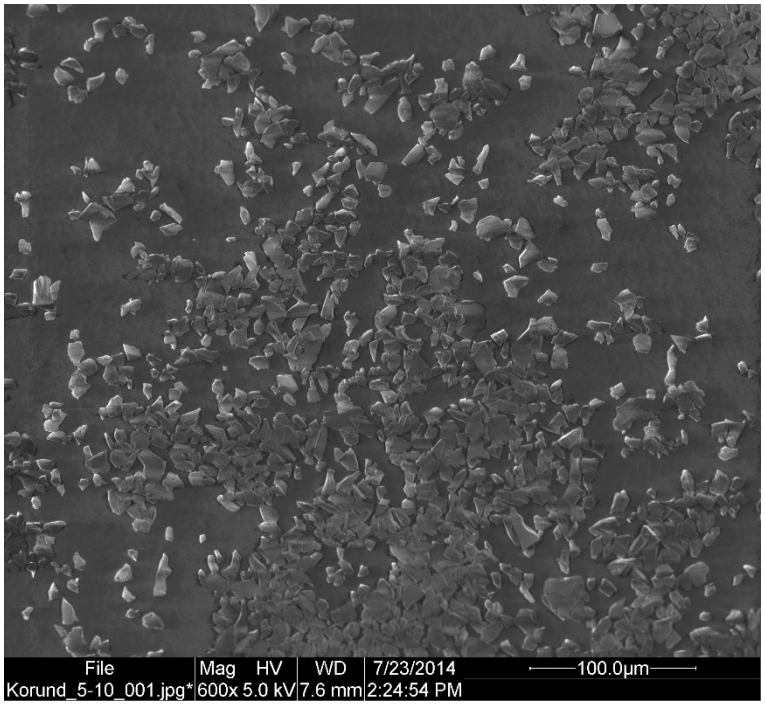

Figure S8 Example SEM image of the corundum CSF II sample powder.

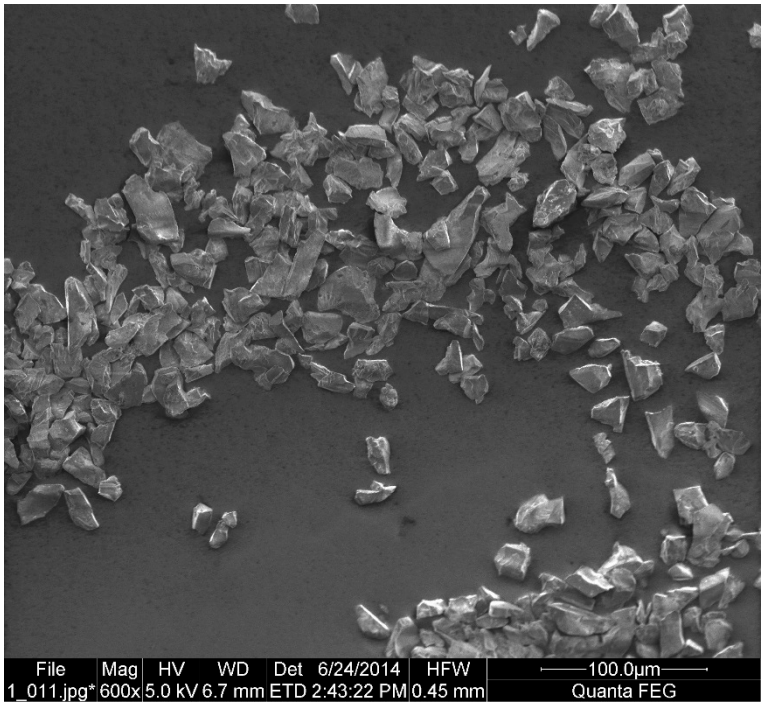

Figure S9 Example SEM image of the corundum CSF IV sample powder.

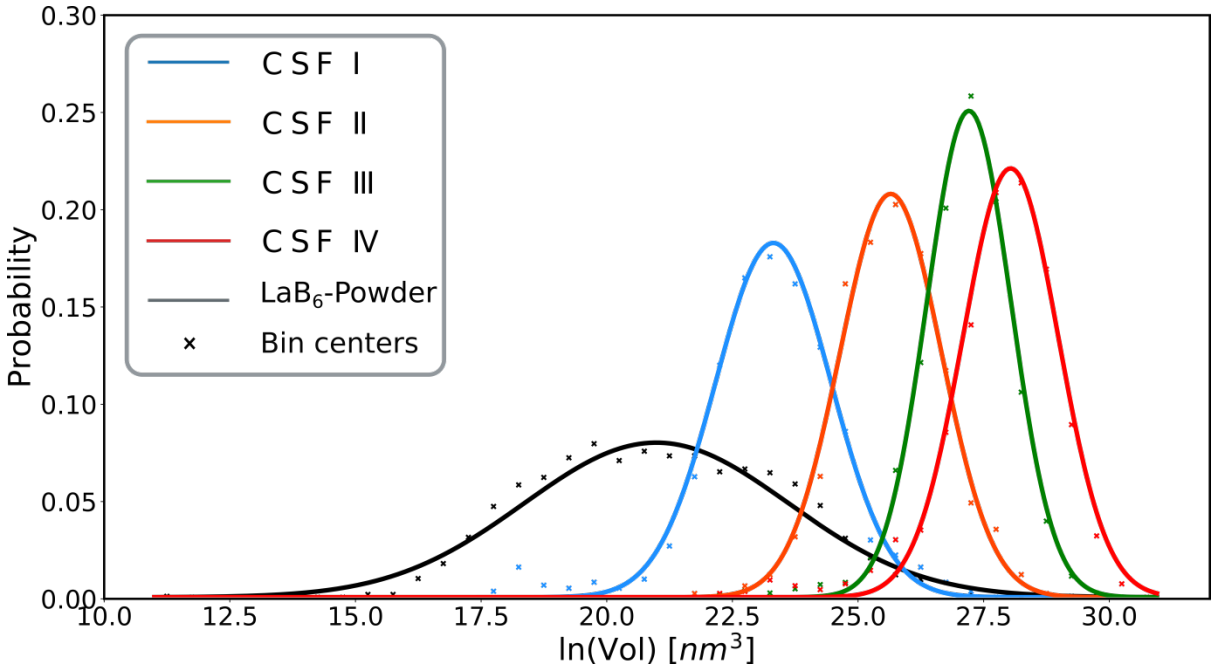

Figure S10 SEM derived volume CSDs of all measured samples. The fitting parameters are presented in Table 5.

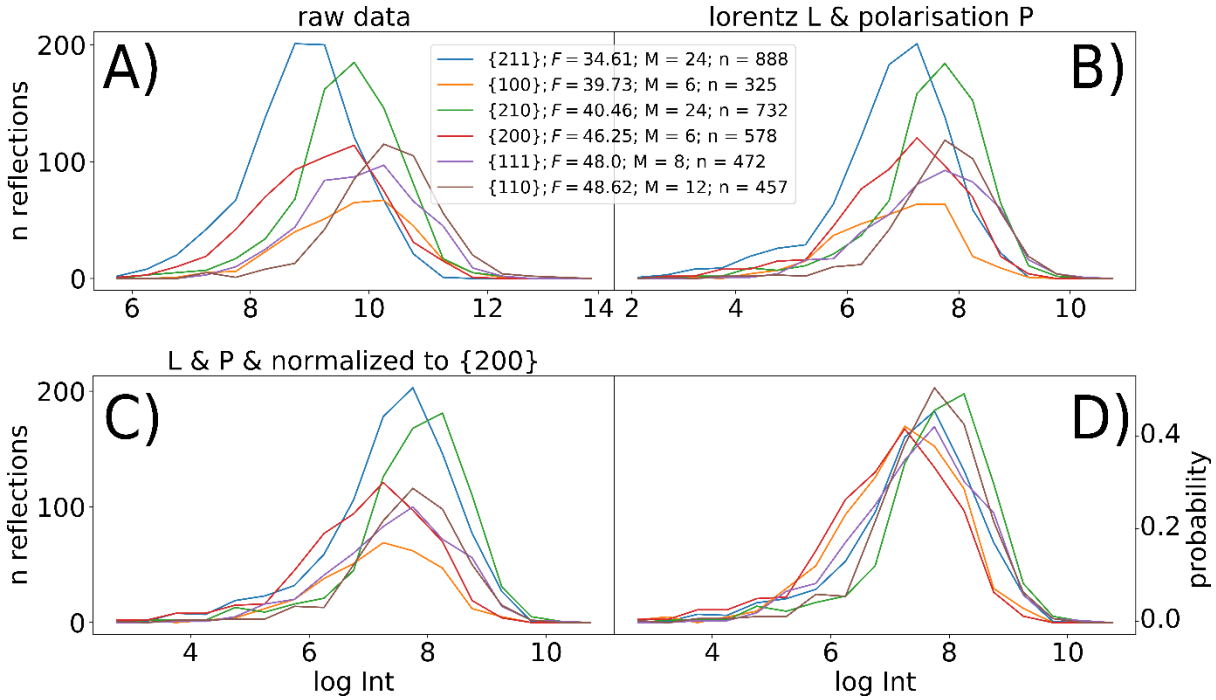

Figure S11 : Subplots A-D of the LaB_6-Powder sample, automatically produced by the *condition()* function. A) shows the uncorrected data, B) the impact of the Lorentz and polarisation factor. C) and D) show the intensity distribution histograms after the intensity correction and internal structure factor normalization: C) shows the number of occurrence representation; D) shows the probability density representation where the number of occurrence in each bin is divided by the total number of occurrence of each IDH. Apparent is that neither sides of the histograms match in position, which on the left side is due to $ID_{cut\text{-}off}$ and on the right side is due to $ID_{exaggeration}$. Although the internal agreement between the different *hkl* is respectable, the results are not trustworthy, as the sizes (obtained with CSFIII as *reference* material) are distinctly higher than the size distribution from SEM observations – see Table 4 of main text).

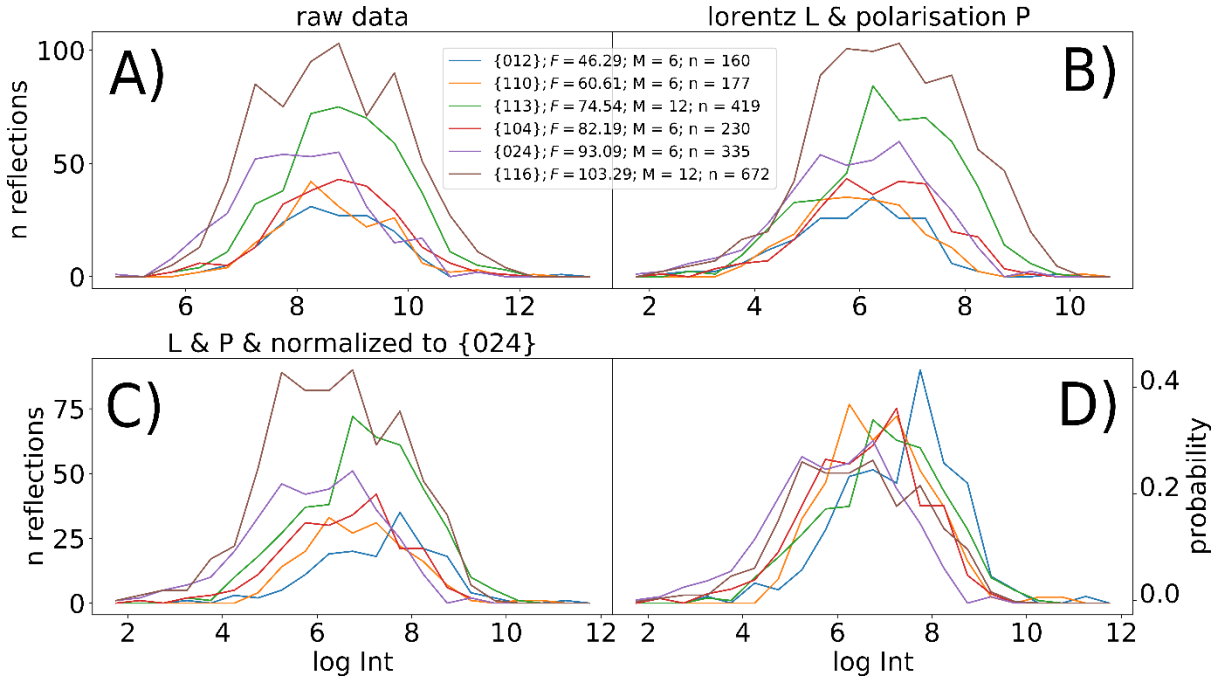

Figure S12: Subplots A-D from CSFI, automatically produced by the *condition()* function. A) shows the uncorrected data, B) the impact of the Lorentz and polarisation factor. C) and D) show the intensity distribution histograms after the intensity correction and internal structure factor normalization: C) shows the number of occurrence representation; D) shows the probability density representation. For the latter the number of occurrence in each bin is divided by the total number of occurrence of each IDH. Apparent is that neither side of the histograms match in position, which on the left side is due to $ID_{cut\text{-}off}$ and on the right side is due to $ID_{exaggeration}$. The number of observations in the legend also reveal $ID_{cut\text{-}off}$. The number of observations should reflect their multiplicities but obviously rather follow their structure factor.

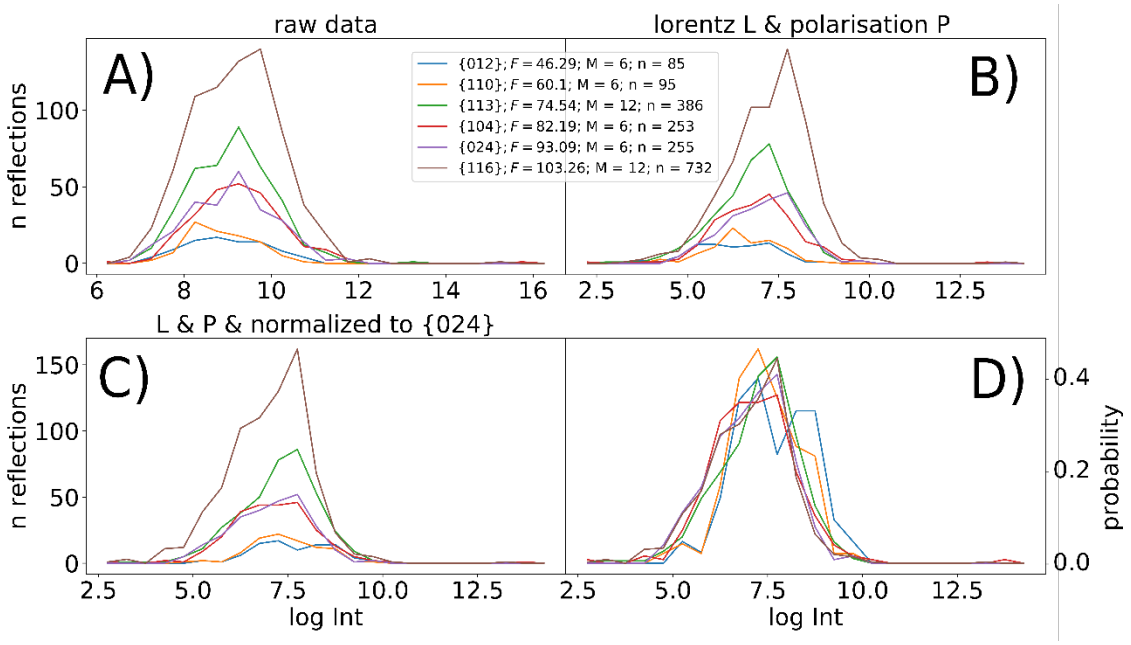

Figure S13 Subplots A-D from CSFII, automatically produced by the *condition()* function. A) shows the uncorrected data, B) the impact of the Lorentz and polarisation factor. Plot C) and D) show the intensity distribution histograms after the intensity correction and internal structure factor normalization: Apparent is that only the stronger reflections match in position. The number of occurrence histogram C) shows the impact of the multiplicity on the number of observations and is partially in agreement with the expectation (see also Table 3). Plot D) shows the probability representation. In both plots, C and D) it is particular evident that the IDHs of the 012 and 110 *hkl*-rings do not match with the other IDHs. In conjunction with the small structure factors of the 012 and 110 hkl-rings this is strong evidence for IDcut-off.

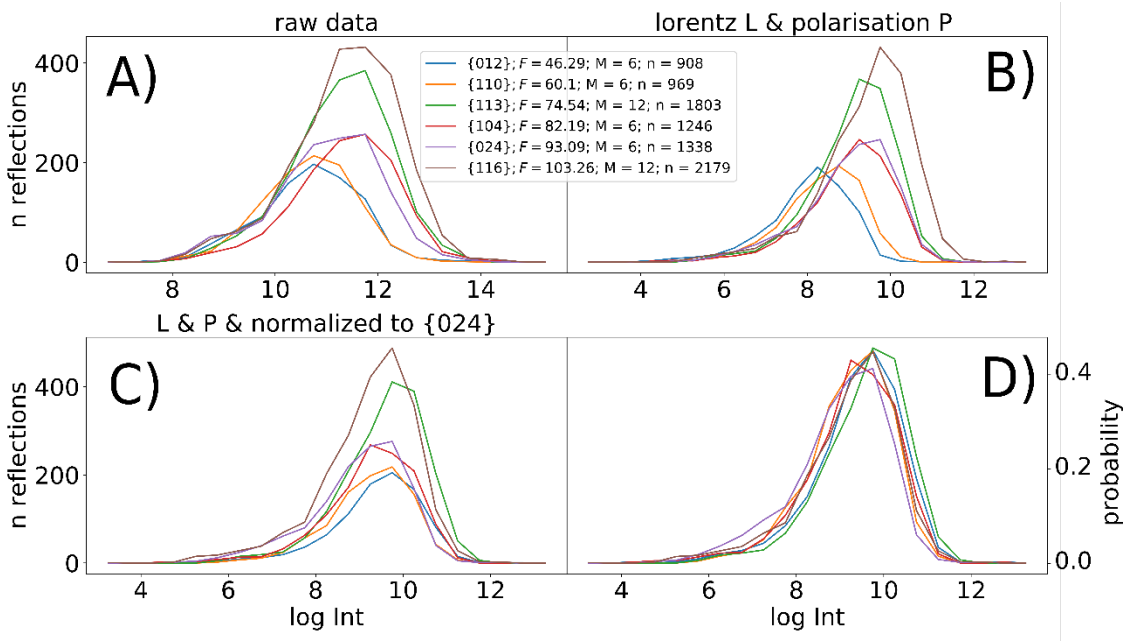

Figure S14 Subplots A-D from CSFIV, automatically produced by the *condition()* function. A) shows the uncorrected data, B) the impact of the Lorentz and polarisation factor. The plots C) and D) show the intensity distribution histograms after the intensity correction and internal structure factor normalization. Apparent is that both sides of the histograms match in position. The number of occurrence histogram, C) shows the impact of the multiplicity on the number of observations and is in good agreement with the expectation (see also Table 3). The plot D) shows the probability representation; here the number of occurrence in each bin is divided by the total number of occurrence of each IDH.

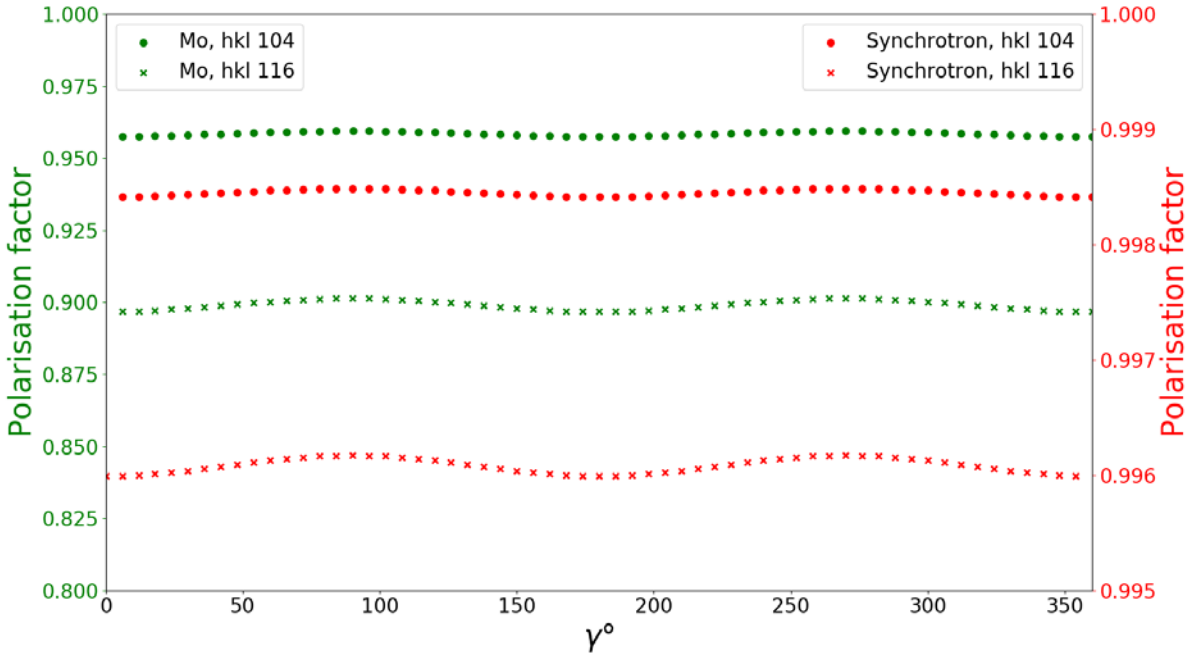

Figure S15 Example calculation of the polarisation factor function graph for two corundum *hkl*-rings and two different X-ray sources. Mo: Molybdenum tube, K_α, λ= 0.71073 Å with graphite monochromator crystal and synchrotron radiation at the ESRF ID 15B with λ= 0.14 Å (Chavanne *et al.*, 1996; Tschentscher & Suortti, 1998).

S2. General conditions on sample edge effect, sampling, and peak overlap

Obtaining spotty diffraction patterns is the key demand of FXD-CSD. In this section we provide a theoretical approach to estimate and test whether the general conditions of FXD-CSD can be met with the used diffractometer setup.

S2.1. Irradiated sample volume and sample edge effect

One requirement of FXD-CSD is to keep the sample edge effect *SEF* low, as the diffracted intensity of crystals only partially irradiated by the incident beam, cannot reflect their true volume. The *SEF* can be estimated with the mean crystal diameter d_{cryst} and its projected area A_{cryst}, and with the incident beam dimensions, expressed as its area A_{beam} and its perimeter P_{beam}. Therefore, *SEF* may be expressed by:

$$SEF = \frac{n_P}{n_A} \quad \text{Eq.S1}$$

With n_A defined as:

$$n_A = \frac{A_{beam}}{A_{cryst}} \quad \text{Eq.S2}$$

And n_P defined as:

$$n_P = \frac{P_{beam}}{d_{cryst}} \quad \text{Eq.S3}$$

In case of polycrystalline materials, crystals on the sample surface are likely to be affected by sample preparation, e.g. being cut by grinding. If this is the case, the sample surface perpendicular to the incident beam direction affected by preparation have to be taken in to account. Generally, we advise the user, that the sample edge effect should not exceed 5% for CSD measurements (10 % to 20% if only the mean crystal size is aimed for).

S2.2. Relationship of Sample statistics, Irradiated sample volume and mean crystal size

CSDs represented as histograms need a large number of observations, to install sufficiently small histogram bins to faithfully represent the distribution. As stated in the main article (see § 3.6) the number of bins needed, can be assured by applying the Freedman-Diaconis rule (Freedman & Diaconis, 1981). To estimate the approximate number of observations n_{obs} , expected within a certain total φ-rotation range φ_{tot} , the approximate irradiated sample volume ISV and the approximate mean crystal size serve as input; randomly orientated crystals are assumed. The total number of crystals n_{tot} in the ISV is simply determined by dividing the ISV with the mean crystal volume; the crystal volume (and the packing factor of powder samples) should be estimated as accurately as possible.

$$n_{obs} = \frac{n_{tot} \sum M_{hkl}\, \varphi_{tot} rad}{4\pi} \qquad \text{Eq.S4}$$

Whether these numbers produce a critical amount of peak overlap on the individual *hkl*-rings is considered in the following section.

S2.3. Ring occupation and overlap

The ring occupation and the expected peak overlap depend on the angular resolution of the diffractometer res_{hkl}, the number of crystals n_{tot} in the ISV and the *hkl*-multiplicity M_{hkl}. $res_{hkl,}$ is depending on the spatial resolution of the detector and the ring radius and is estimated concerning the resolution in the φ-rotation direction and along the used *hkl*-ring:

$$res_{hkl} = n_{\varphi\text{-}steps}\, \varphi_{\text{step}}\text{rad}\ n_{pix}\, (\frac{1}{r_{ring}}) \qquad \text{Eq. S5}$$

with r_{ring} in pixels and the distance between the reflection maxima in both directions, $n_{\varphi\text{-}steps}$ and n_{pix}. Values for $n_{\varphi\text{-}steps}$ and n_{pix} depend on the peak spread on the detector (depending on the resolution function of the diffractometer, the crystal size, and quality); with the setup described in the main article, using twice the peak spread has turned out to give reasonable results. With that the probability *P* of having overlap can be calculated. Using the number of possible orientations n_{pos} and the given number of crystals n_{tot} in the ISV, one obtains

$$P = \frac{1}{n_{pos}}\, n_{tot} = 1/(\frac{4\,\pi}{M_{hkl}\, res_{diff}})\, n_{tot} \qquad \text{Eq. S6}$$

S2.3.1. Accidental overlap

Accidental full overlap arising from crystals with the same orientation cannot be resolved or detected by the software and therefore cannot be discarded. To estimate its portability of occurrence the equations Eq. S5 and S6 can be used. To do this one only needs to set $n_{\varphi\text{-}steps}$ and n_{pix} to 4, the minimum distance what can be resolved by the software. For example using the setup described in §3.3 of the main article with an ISV of ~ 0.125 mm³ and having about 20.000 crystals in it, gives a chance of 0.37 that accidental full overlap is happening once on a *hkl*-ring with the multiplicity of 10, hence is neglectable small.

S3. Intensity corrections

S3.1. Absorption

Attenuation affects depend on the linear absorption coefficient (μ) and the path length the X-ray radiation travels through the crystal; together they define the transmission factor A_{hkl}. μ is known because it is material and wavelength specific. The path length has to be estimated because in the case

of FXD-CSD neither the shape nor the exact individual crystal size is a known property. Therefore A_{hkl} can only be estimated for the average crystal size in each bin of the CSD histogram by assuming a spherical crystal shape and can be calculate by an analytical expression (Rouse *et al.*, 1970).

$$A_{hkl} = e^{-(a_1+b_1 \sin^2\theta)\mu r-(a_2+b_2 \sin^2\theta)(\mu r)^2} \quad \text{Eq.S 7}$$

With r the crystal radius and the coefficients a_1 = 1.5108, b_1=-0.03145, a_2=-0.0951 and b_2=-0.2898 (Rouse *et al.*, 1970).

For the *reference* measurement the correction can only be applied in an iterative procedure because the intensity derived *reference* CSD, needed to estimate the crystal path length 2r, is obtained by the S1 scaling, which changes when the correction is applied to the *reference* ID. For this reason, the correction is considered to be self-correlated and must be bounded to be self-consistent. The used bound is a distribution shape match between the intensity derived CSD and the *reference* volume CSD, derived *via* SEM imagery. In the first iteration cycle S1 is determined and used to calculate the CSD derived from the ID. Calculating the transmission factors with the size information obtained (r) and applying it to the ID, changes the shape of the ID what again changes the S1 scaling factor. The altered scaling factor is used for the second iteration. Ideally the iterations are carried out until the ID shape matches the shape of the SEM derived volume CSD. To perform the correction in this manner the CSD of the *reference* must be beyond doubt which is up to now not necessarily the case (see §5.3). In practice it turned out that for the used reference materials (LaB_6 (Nützmann, 2013) and corundum) the change in crystal size is well below 2% in the first iteration cycle. Thus, without a better reference material, the correction is not considered to improve the results and therefore not applied.

The correction of the sample material ID is straightforward. A_{hkl} could be calculated for the obtained crystal sizes and used for a correction.

S3.2. Beam profile deconvolution

S3.2.1. Theory

In the theoretical consideration of measuring the grain size with X-ray diffraction a lateral homogenous, boxed shaped beam is assumed. In practice, especially in the case of lab equipment and collimators with big diameters, this is not necessarily the case (Figure S16). Inhomogeneities broaden the measured intensity distributions and blur the relationship between crystal size and measured intensity. Mathematically this corresponds to a convolution. In a dataset convolved like this, one cannot tell the difference between a small crystal diffracting in a high intensity region, from a bigger crystal diffracting in a low intensity region.

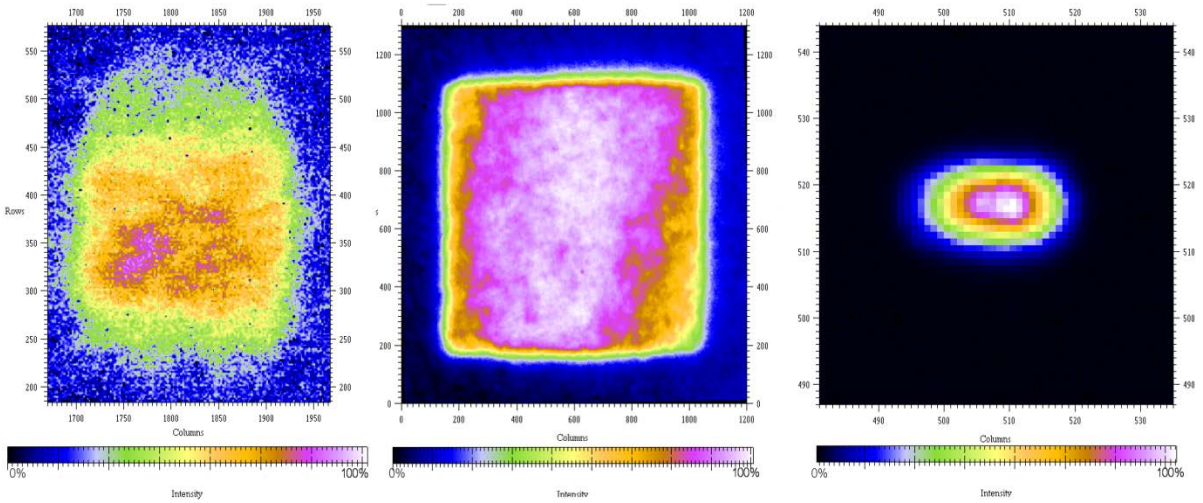

Figure S16 Examples for lateral profiles of primary X-ray beams. Left: ESRF ID15. Middle: DESY Petra III P08. Right: Bruker Apex II 0.5 Collimator.

The position of each crystal in the incident beam is statistically uncorrelated with the CSD and therefore a correction for the non-uniform beam intensity can be applied *via* a mathematical deconvolution. For this a discrete intensity histogram over log-intensity of the primary beam is created. In the following the nomenclature of signal processing is used. The intensity histogram $f(x)$ of the initial beam is the representation of the filter and the measured diffracted intensity distribution histogram (IDH) $s(x)$ the representation of the signal. The sought information is the true IDH $g(x)$. The Convolution $f(x) * g(x)$ – occurring while measuring – is written as follows (Wikipedia contributors, 2017):

$$(f * g)(i) \int_{-\infty}^{\infty} g(i)\, f(i-j)\, dj \qquad \text{Eq. S8}$$

The variable j is inverting the order of f. Since the data available in this case is not continuous the convolution is sufficiently described by a discrete form (Wikipedia contributors, 2017) :

$$(f * g)[i] := \sum_{j=-k}^{k} g[j] f[i-j] \qquad \text{Eq. S9}$$

To perform the deconvolution the beam profile $f(x)$ and the measured ID $s(x)$ need to be known and converted to a usable from. The beam profile can be measured either with a high-resolution X-ray photo film and scanned afterward or measured directly with a 2D detector. The direct measurement can only be done with lab sources because it is easily possible to lower its intensity by using minimal current (5 mA); otherwise it is likely to damage the detector. Since FXD-CSD uses a statistical approach to determine the CSD and the measured ID $s(x)$ is just a representation of it, the beam profile is only needed as relative measure and hence can be represented by an intensity histogram. The number and the size of the histogram bins need to have the same size as the measured ID. Once the filter $f(x)$ is

converted in to a histogram and written as matrix $F_{ij} = f[i-j]$, the convolution can be - in conformity with eq. ES4 - written as matrix multiplication:

$$S_i = \sum_{j=-k}^{k} F_{ij} g_j \qquad \text{Eq. S10}$$

The least square solution for g_j minimizes $\sum_i (S_i - \sum_j F_{ij} g_j)^2$, which corresponds to a vanishing derivative with respect to g_r:

$$\sum_i F_{ir}(S_i - \sum_j F_{ij} g_j) = F^T s - F^T F g = 0 \qquad \text{Eq. S11}$$

What can be solved for g:

$$g = (F^T F)^{-1} F^T s \qquad \text{Eq. S12}$$

The problem when solving for g_j by least squares is that the result can be wiggly and needs to be regulated. We are looking for a smooth solution, hence we penalize curvature. To achieve this we minimizes both, least square deviation and to some measure (λ multiplier) the ruggedness of the curve. This could be for example the curvature term $\mathrm{c_i} = \mathrm{g_{i-1}} + \mathrm{g_{i+1}} - 2g_i$. Hence a suitable function is

$$\sum_i (S_i - \sum_j F_{ij} g_j)^2 + \lambda \sum c_i^2 = \sum_i (S_i - \sum_j F_{ij} g_j)^2 + \lambda \sum_i (g_{i-1} + g_{i+1} - 2g_i)^2$$

The curvature term can be expressed as a matrix multiplication $c_i = \sum_j D_{ij} g_j$ with $D_{ii} = -2$, $D_{i,i-1} = 1$, $D_{i,i+1} = 1$, but the boundaries $i = -k$ and $i = k$ need to be modified. The curvature term is then $\sum_i c_i^2 = \sum_{ijl} g_l D_{il} D_{ij} g_j$. Again, to minimize we differentiate with respect to g_r and set the derivative to zero:

$$0 = \sum_i F_{ir} \left(s - \sum_j F_{ij} g_j \right) + \lambda \sum_{ij} D_{ik} D_{ij} g_j$$
$$= F^T s - F^T F g + \lambda D^T D g = F^T s - (F^T F - \lambda D^T D) g$$

Now this can be solved for g by inverting the matrix $(F^T F - \lambda D^T D)$.

$$g = (F^T F - \lambda D^T D)^{-1} F^T s$$

This is done by the *solver.qp* function of the *cvxopt* (Andersen *et al.*, 2013) python package.

S3.2.2. Example deconvolution

Before the deconvolution can be performed the primary beam profile (the filter) is converted into log space, normalized to the maximum bin value of the ID and, converted into a histogram with bins the

same size like the ID (Figure S17). While the high-end value of the beam profile is clearly defined by the highest pixel value, the lower end of the primary beam profile intensity distribution is not clearly defined. The low end is somewhere between the background of the measured beam profile and some fraction of the lowest measured crystal intensity. To determine where the cut-off threshold – the low intensity end of the filter – is to be placed (a multiple of the step size in log space) two measures are used: 1) The deviation between the volume distribution of the reference material and the deconvoluted measured ID, which should be as small as possible (Figure S18) and 2) the deviation between the measured ID and the re-convolved signal. For the latter the deconvolution is reversed (re-convoluted) to check whether the former signal is reproduced. The deviation should be as small as possible. Both measures are used for optimizing the cut-off threshold. If the automated threshold determination is not working a value can be set manually.

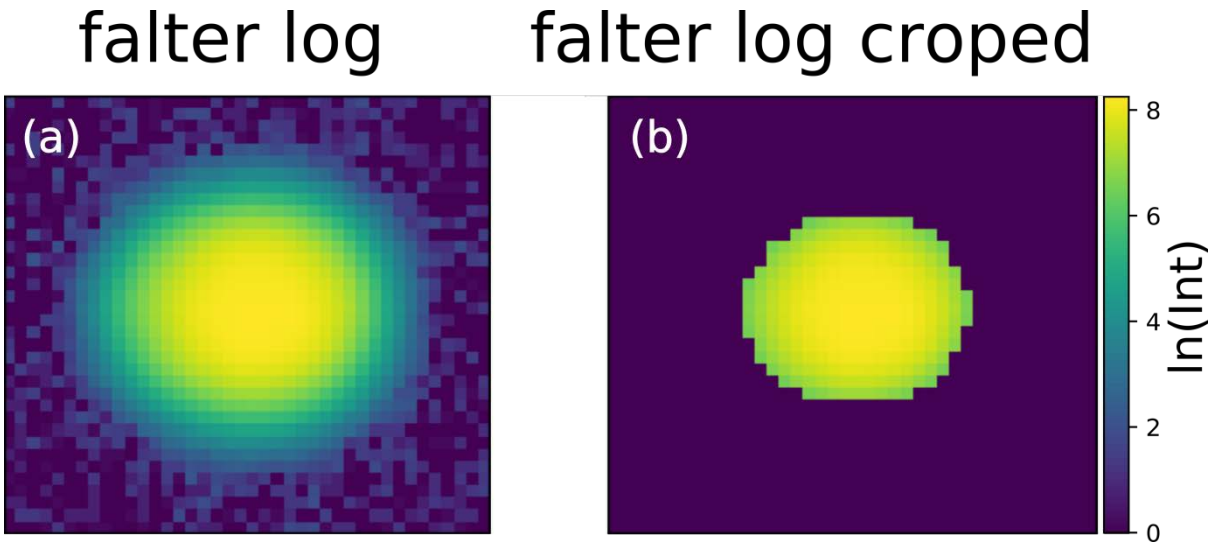

Figure S17 Lateral beam profile, recorded with a Bruker Apex II detector. A 0.5 mm pinhole collimator was used. a) log space representation of the lateral beam profile. b) log space representation of the lateral beam profile after applying the cut-off threshold. The threshold level is variable and refined during the deconvolution process.

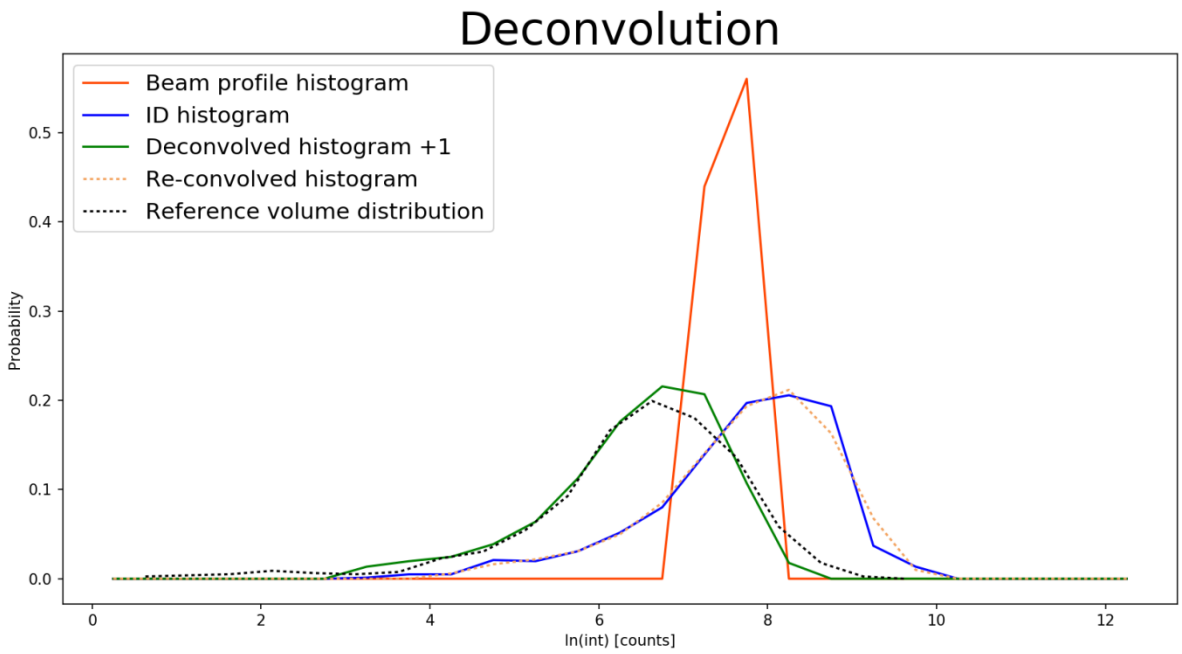

Figure S18 Exemplary deconvolution plot, showing the beam profile histogram [WFK1](orange line) and the intensity distribution histogram (blue line). The green line is showing the deconvolved histogram. To verify the results and to determine the beam profile cut-off threshold the deconvolved histogram is compared with the reference volume distribution; this is possible because the volume distribution is known. A second test showing the success of the deconvolution is to compare the initial intensity distribution (blue line) with the reconvolved intensity distribution (dotted black line). The reconvolved histogram (orange dotted line) is obtained by convoluting the deconvolved histogram with the beam profile histogram and has to match the initial intensity distribution histogram.

In practice it turned out, that the ID convolution has not a strong influence on the resulting CSDs, which is generally smaller than the uncertainties originating from uncertainties of the reference volume distribution. In case of the smaller grain size fractions presented in § 4 of the main article, the fitted half width at half maxima (HWHM) of the IDs are smaller than the HWHM of the reference volume CSDs. This is not true for the bigger grain size fraction – which was one reason for implementing the deconvolution – but turned out to originate from evolving satellite peaks (see § 4 in the main article) not from beam inhomogeneities.

S4. Crystal size fraction separation *via* sedimentation

To obtain a consecutive series of crystal size fractions (CSF) to verify the FXD-CSD method a corundum blasting abrasive powder (Edelkorund F 120, Kuhmichel Abrasiv GmbH) is used as starting material. The material is grinded in a mortar and separated into several CSFs *via* sedimentation in water. A so called Atterberg cylinder, a glass cylinder with a faucet a few cm above the bottom and a filling

mark at the top, is used to separate the following nominal CSFs: <2 µm, 2 - 5 µm, 5 – 10 µm, 10 - 15 µm, 15 – 20 µm, 20 – 25 µm, 25 – 35 µm, 35 - 40 µm, 40 – 45 µm. The 2 – 5 µm, 5 - 10 µm, 10 - 15 µm and 15 - 20 µm CSFs, called CSD I-IV, are presented here. The cylinder is filled with water to a certain level (filling mark) and the bulk powder is given in the cylinder and closed with a lid. After rocking the cylinder until the whole sample is floating the cylinder is put aside upright. After a certain time, calculated *via* Stokes law fed with the crystal size to be separated and the water column height, the faucet is opened and the water is collected (for further information see Müller, 1967). The collected water contains only crystals smaller than the size used for the calculation of the sedimentation duration. The sediment on the bottom and the suspension below the faucet level contain the bigger crystals and parts of the smaller CSF; at the beginning of each separation step the crystals are evenly distributed in the water column, therefore the fall distance is not the same for all particles and parts of the small fraction will sediment during the calculated time period. To separate the majority of the small CSF the procedure is carried out several times (up to ten times for the smallest fractions).

S5. Satellite peaks

Besides the samples presented (CSF I-IV) in the main article several other samples with bigger mean crystal sizes have been produced (see § S3) and characterized with SEM imagery. The subsequent FXD-CSD data analysis revealed that with increasing crystal size, artificial satellite peaks evolve on the detector which wander through their main peaks (see Figure S19). This problem did occur several times in the past when using our diffractometer (Bruker AXS Apex II CCD diffractometer (D8 Base) with a molybdenum tube and graphite monochromator) to measure large single crystals; it was also observed while performing calibration measurements carried out with a spherical Ylid crystal used as intensity standard provided by the diffractometer manufacturer. The most likely explanation for this artefact is a deficient monochromator crystal which produces small amounts of crossfire radiation. Even though a mending work around is implemented in our software – suppressing peaks close together by increasing the minimum distance parameter (*min_distance* of the *pickpeaks*() function) of the software – we decided to only present data sets which are not or only slightly affected in the main article.

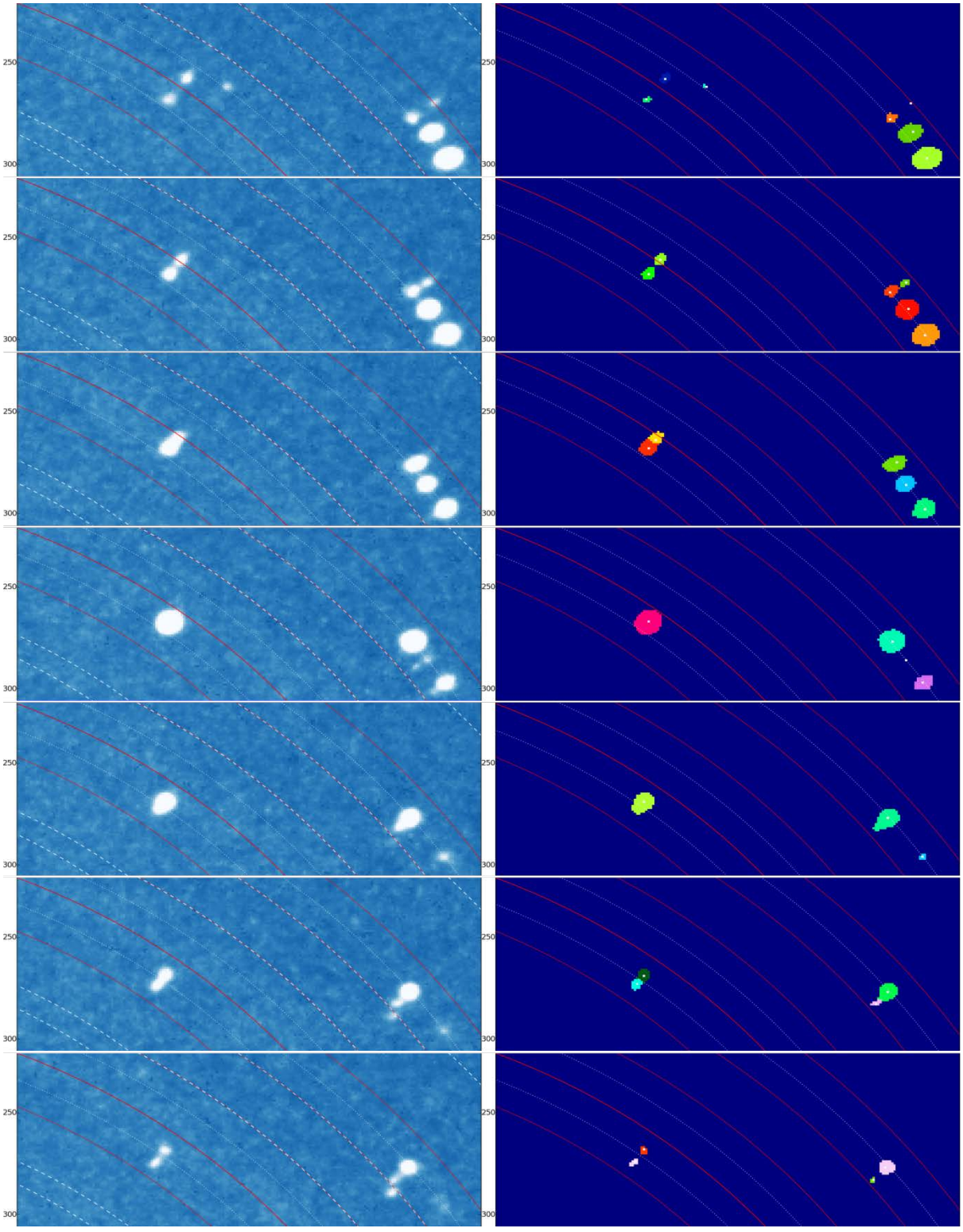

Figure S19 Exemplary frame sections from a stepwise rotation measurement showing the evolution (top down) of satellite peaks (left) and how they are detected by the software. The appearance of satellite peaks is increasing with crystal size. For the CSF I – IV, the smallest crystal size fractions, the appearance is low and its detection is suppressed by increasing the *min_distance* parameter of the software. This parameter controls the minimum distance allowed between two neighbouring peaks detected in the frames. If the distance between two peaks is smaller, the weaker peak is ignored.

S6. Data evaluation

The rocking curves of each reflection can be evaluated using their central moments, which than can be used as rejection criteria. These are: Weighted-mean $\acute{x}$, -variance *Var*, -skewness γ, and -kurtosis γ_2, describing the mean position, peak spread, the asymmetry of the curve and the flatness or peakedness, respectively (see §3.4 3rd Step).

$$\acute{x} = \frac{1}{w}\sum_{n}^{i=1} x_i w_i$$

$$Var = \frac{1}{n-1}\sum_{n}^{i=1} w_i(x_i - \acute{x})$$

$$\gamma = \frac{n(n+1)}{(n-1)(n-2)}\sum_{n}^{i=1} w^{\frac{3}{2}}\left(\frac{x_i - \acute{x}}{s}\right)^3$$

$$\gamma_2 = \frac{n(n+1)}{(n-1)(n-2)(n-3)}\sum_{n}^{i=1} w_i^2\left(\frac{x_i - \acute{x}}{s}\right)^4 - \frac{3(n-1)^3}{(n-2)(n-3)}$$

References for Supporting Information:

Andersen, M. S., Dahl, J. & Vanderberghe, L. (2013). CVXOPT: A Python package for convex optimization. cvxopt.org.

Chavanne, J., Elleaume, P. & Van Vaerenbergh, P. (1996). *Rev. Sci. Instrum.* **67**, 3346.

Freedman, D. & Diaconis, P. (1981). *Zeitschrift Für Wahrscheinlichkeitstheorie und Verwandte Gebiete*. **57**, 453–476.

Müller, G. (1967). Methods in sedimentary petrology E. Schweitzerbart'sche Verlagsbuchhandlung.

Nützmann, K. (2013). Crystallite Size Distributions of CH 4 -CO 2 Gas Hydrates from Diffraction Data (Including the Effect of Absorption). MSc. Thesis. University of Göttingen.

Rouse, K. D., Cooper, M. J., York, E. J. & Chakera, A. (1970). *Acta Crystallogr. Sect. A.* **26**, 682–691.

Tschentscher, T. & Suortti, P. (1998). *J. Synchrotron Radiat.* **5**, 286–292.

Wikipedia contributors (2017). Convolution. https://en.wikipedia.org/wiki/Convolution.